Early X-ray and optical observations of the soft gamma-ray repeater SGR 0418+5729

P. Esposito,[1,2]⋆ G. L. Israel,[3] R. Turolla,[4,5] A. Tiengo,[1] D. Götz,[6] A. De Luca,[1,7] R. P. Mignani,[5] S. Zane,[5] N. Rea,[8] V. Testa,[3] P. A. Caraveo,[1] S. Chaty,[6] F. Mattana,[9] S. Mereghetti,[1] A. Pellizzoni[10] and P. Romano[11]

[1]*INAF/Istituto di Astrofisica Spaziale e Fisica Cosmica - Milano, via E. Bassini 15, I-20133 Milano, Italy*
[2]*INFN - Istituto Nazionale di Fisica Nucleare, sezione di Pavia, via A. Bassi 6, I-27100 Pavia, Italy*
[3]*INAF/Osservatorio Astronomico di Roma, via Frascati 33, I-00040 Monteporzio Catone, Italy*
[4]*Università di Padova, Dipartimento di Fisica, via F. Marzolo 8, I-35131 Padova, Italy*
[5]*Mullard Space Science Laboratory, University College London, Holmbury St. Mary, Dorking, Surrey RH5 6NT*
[6]*AIM (UMR 7158 CEA/DSM-CNRS-Université Paris Diderot) Irfu/Service d'Astrophysique, Saclay, FR-91191 Gif-sur-Yvette Cedex, France*
[7]*IUSS - Istituto Universitario di Studi Superiori, viale Lungo Ticino Sforza 56, I-27100 Pavia, Italy*
[8]*Institut de Ciències de l'Espai (CSIC–IEEC), Campus UAB, Facultat de Ciències, Torre C5-parell, E-08193 Barcelona, Spain*
[9]*Laboratoire AstroParticule et Cosmologie, Université Paris 7 - Denis Diderot, rue A. Domon et L. Duquet 10, FR-75205 Paris, France*
[10]*INAF/Osservatorio Astronomico di Cagliari, località Poggio dei Pini, strada 54, I-09012 Capoterra, Italy*
[11]*INAF/Istituto di Astrofisica Spaziale e Fisica Cosmica - Palermo, via U. La Malfa 153, I-90146 Palermo, Italy*

ABSTRACT

Emission of two short hard X-ray bursts on 2009 June 5 disclosed the existence of a new soft gamma-ray repeater, now catalogued as SGR 0418+5729. After a few days, X-ray pulsations at a period of 9.1 s were discovered in its persistent emission. SGR 0418+5729 was monitored almost since its discovery with the *Rossi X-ray Timing Explorer* (2–10 keV energy range) and observed many times with *Swift* (0.2–10 keV). The source persistent X-ray emission faded by a factor of ∼10 in about 160 d, with a steepening in the decay about 19 d after the activation. The X-ray spectrum is well described by a simple absorbed blackbody, with a temperature decreasing in time. A phase-coherent timing solution over the ∼160 d time-span yielded no evidence for any significant evolution of the spin period, implying a 3σ upper limit of 1.1×10^{-13} s s^{-1} on the period derivative and of $\sim 3 \times 10^{13}$ G on the surface dipole magnetic field. Phase-resolved spectroscopy provided evidence for a significant variation of the spectrum as a function of the stellar rotation, pointing to the presence of two emitting caps, one of which became hotter during the outburst. Finally, a deep observation of the field of SGR 0418+5729 with the new Gran Telescopio Canarias 10.4-m telescope allowed us to set an upper limit on the source optical flux of $i' > 25.1$ mag, corresponding to an X-ray-to-optical flux ratio exceeding 10^4, consistent with the characteristics of other magnetars.

Key words: stars: neutron – pulsars: general – X-rays: individual: SGR 0418+5729.

1 INTRODUCTION

Soft gamma-ray repeaters (SGRs) form a small class of sources which emit short (∼0.1 s) bursts of soft gamma rays with peak luminosities of $\sim 10^{41}$–10^{42} erg s^{-1}. Originally believed to be a subclass of the gamma-ray bursts (GRBs), they were soon recognized as a different population because their bursts repeat and are quite soft, at variance with canonical GRBs. Apart from the flaring activity, sometimes culminating in dramatic, very energetic giant flares

with peak luminosity exceeding 10^{46} erg s^{-1} (as was the case of the 2004 event from SGR 1806–20; Hurley et al. 2005), SGRs display persistent emission from 0.1 to hundreds of keV, with pulsations of several seconds ($P \sim 2$–9 s), rapid spin-down ($\dot{P} \sim 10^{-11}$ s s^{-1}) and significant variability in period derivative, pulse shape, flux and spectral shape.

This phenomenology has been interpreted within the context of the magnetar model (Duncan & Thompson 1992; Paczynski 1992; Thompson & Duncan 1995, 1996). SGRs are in fact believed to be young, isolated neutron stars endowed with an ultrahigh magnetic field ($B \sim 10^{14}$–10^{15} G), which is thought to be the ultimate energy reservoir for their activity. It is now commonly accepted

⋆E-mail: paoloesp@iasf-milano.inaf.it

that anomalous X-ray pulsars (AXPs), a peculiar class of pulsating X-ray sources, are also magnetars, in view of the many similarities in their persistent and bursting emission (see Woods & Thompson 2006; Mereghetti 2008 for recent reviews).[1]

On 2009 June 5, a new SGR, namely SGR 0418+5729, was discovered, thanks to the detection of two short X-ray bursts with the *Fermi* Gamma-ray Burst Monitor (GBM) and other hard X-ray instruments (van der Horst et al. 2009, 2010). After a few days, on 2009 June 10, X-ray pulsations at a period of 9.1 s were discovered in the persistent emission with *Rossi X-ray Timing Explorer* (*RXTE*), further supporting the magnetar nature of the source (Göğüş, Woods & Kouveliotou 2009a). Ground-based follow-up observations in optical and infrared wavebands (discussed in the following), as well as at radio wavelengths (with the 100-m Green Bank Telescope; Lorimer et al. 2009), failed to detect the source.

Here we report on the analysis of a series of observations carried out in the soft X-ray range (1–10 keV) by the X-Ray Telescope (XRT) aboard *Swift* and by the Proportional Counter Array (PCA) instrument of the *RXTE* satellite, collected in the period from 2009 June 11 to 2009 November 24. We also present the results of a very deep optical observation performed on 2009 September 15 with the new Gran Telescopio Canarias (GTC) 10.4-m telescope on La Palma (Canary Islands, Spain), which is presently the largest single-aperture optical telescope in the world.

2 OBSERVATIONS AND DATA REDUCTION

2.1 *Swift*

The XRT (Burrows et al. 2005) on-board *Swift* uses a CCD detector sensitive to photons between 0.2 and 10 keV with an effective area of about 110 cm^2 and a field of view (FOV) of 23 arcmin diameter. Several observations of SGR 0418+5729 were performed following its discovery, in both photon counting (PC) and windowed timing (WT) modes. In the PC mode the entire CCD is read every 2.507 s, while in the WT mode only the central 200 columns are read and only one-dimensional (1D) imaging is preserved, achieving a time resolution of 1.766 ms (see Hill et al. 2004 for more details). Table 1 (see also Fig. 1) reports the log of the observations that were used for this work.

The data were processed with XRTPIPELINE (version 0.12.3, in the HEASOFT software package[2] 6.6), and standard filtering and screening criteria were applied by using FTOOLS tasks. We extracted the PC source events from a circle with a radius of 20 pixels (1 pixel corresponds to about 2.36 arcsec) and the WT data from a 40 × 40 pixel^2 box along the image strip. To estimate the background, we extracted PC and WT events from source-free regions far from the position of SGR 0418+5729.

For the timing analysis, the photon arrival times were converted to the Solar system barycentre with the BARYCORR task and using the *Chandra* source position (RA = 04^{h}18^{m}33^s.867, Dec. = +57°32′22″.91, epoch J2000; 0.35 arcsec accurate) provided by Woods et al. (2009b). For the spectral fitting, the ancillary response files (arf) were generated with XRTMKARF, and they account for different extraction regions, vignetting and point spread func-

Table 1. Journal of the *Swift*/XRT observations of SGR 0418+5729. The complete observation sequence number is prefixed by 00031422 followed by the three-digit segment number given here (e.g. 00031422001).

Sequence/mode	Start/End time (UT) yyyy-mm-dd hh:mm		Exposure[a] (ks)
001/PC	2009-07-08 20:52	2009-07-08 22:54	2.9
002/PC	2009-07-09 00:07	2009-07-09 19:29	10.6
003/PC	2009-07-10 00:17	2009-07-10 07:01	5.6
004/WT	2009-07-12 00:29	2009-07-12 15:04	7.1
006/WT	2009-07-15 15:16	2009-07-15 23:40	7.7
007/WT	2009-07-16 00:55	2009-07-16 23:36	16.4
008/PC	2009-09-20 21:11	2009-09-21 23:04	9.4
009/PC	2009-09-22 00:46	2009-09-22 23:28	7.6
010/PC	2009-11-08 00:38	2009-11-08 23:03	15.1

[a]The exposure time is usually spread over several snapshots (single continuous pointings of the target) during each observation.
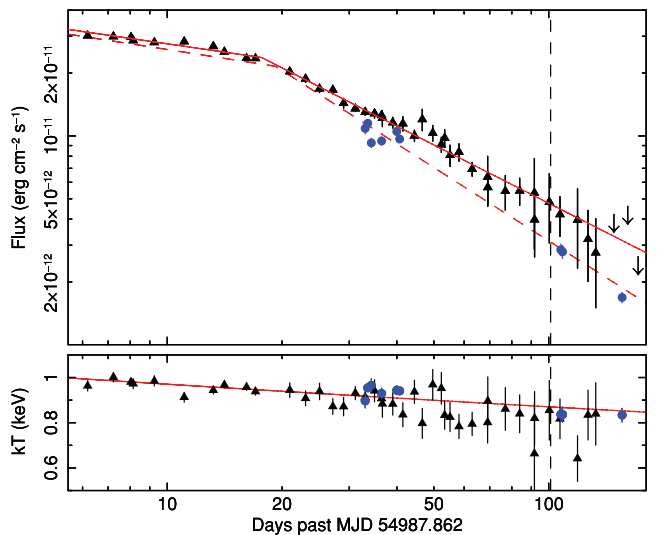

Figure 1. Top panel: the outburst decay of the persistent X-ray flux of SGR 0418+5729 as seen by *RXTE* (black filled triangles) and *Swift* (blue filled circles). We assumed as $t = 0$ MJD 54987.862, which is the time of the detection of the first burst. The fluxes are absorbed and in the 2–10 keV energy range; the down-arrows indicate upper limits at the 3σ confidence level. The broken power law describing the *RXTE* flux decay is superimposed in red (solid line); we also plotted (red, dashed line) the simultaneous fit of the *Swift* and *RXTE* data after subtracting a constant flux from the latter (see Section 3.2). Bottom panel: evolution of the characteristic temperature of the blackbody model inferred from the spectral fitting. The power-law model describing the decay of the blackbody temperature (see Section 8) is plotted in red (solid line). The vertical dashed lines indicate the epoch of the observation with the GTC (see Section 6).

tion corrections. We used the latest available spectral redistribution matrix (rmf) in CALDB (v011).

2.2 *RXTE*

The PCA (Jahoda et al. 1996) on-board *RXTE* consists of an array of five collimated xenon/methane multianode Proportional Counter Units (PCUs) operating in the 2–60 keV energy range, with a total effective area of approximately 6500 cm^2 and a full width at half-maximum (FWHM) FOV of about 1°. The 46 *RXTE*/PCA observations of SGR 0418+5729 (Obs. ID: 94048) reported here span

from 2009 June 11 to 2009 November 24 (see Fig. 1). The exposures range from 0.6 to 13.6 ks, for a total of 194.2 ks.

Raw data were reduced using the FTOOLS package. To study the timing properties of SGR 0418+5729, we restricted our analysis to the data in the Good Xenon mode, with a time resolution of 1 μs and 256 energy bins. After correction to the Solar system barycentre with the FXBARY task, the event-mode data were extracted in the 2–10 keV energy range from all active detectors (in a given observation) and all layers, and binned into light curves of 0.1 s resolution.

For the spectral analysis, we have only made use of the Standard 2 data (time resolution of 16 s and 128 energy bins) from PCU-2, which is the best-calibrated PCU in the PCA, and spectra were extracted including only top-layer events. Good time intervals were selected to ensure stable pointing and filter out electron contamination events, following the standard procedure for faint sources. Response matrices (combining rmf and arf files) were generated using PCARSP. Background subtraction for PCA data is performed using a synthetic model that accounts for the time-variable particle background and for the average cosmic X-ray background (see Jahoda et al. 2006 for details). Possible Galactic diffuse emission remains in the background-subtracted data, as well as emission from any X-ray source that occurs in the instrument FOV.

3 SPECTRAL ANALYSIS

Because of its non-imaging nature and wide FOV, the *RXTE*/PCA instrument is not well suited for the spectral study of relatively faint and soft sources such as SGR 0418+5729. The *Swift*/XRT instrument, instead, offers a good sensitivity and ensures proper background subtraction (also in the case of WT observations). For this reason, we started the spectral analysis by working only with the *Swift*/XRT data.

3.1 *Swift*/XRT

The observations carried out within a few days and in which the count rates were similar were added in order to accumulate sufficient statistics for meaningful spectral fits; as a result, we obtained four spectra: 001–003, 004–007 (WT data), 008–009 and 010 (see Table 1). The spectral channels were then grouped to have bins with a minimum number of 30 photons. The spectral fitting, with the XSPEC analysis package (version 12.4; Arnaud 1996), was performed in the 0.7–10 keV energy range, since the very few counts from SGR 0418+5729 made the data below 0.7 keV useless.

We first tried fitting simple models to the spectra: a power law, a blackbody, a double blackbody and a blackbody plus power law,

all modified for interstellar absorption. The abundances used are those of Anders & Grevesse (1989) and photoelectric absorption cross-sections are from Balucinska-Church & McCammon (1992). We fit all spectra simultaneously with the hydrogen column density tied up between the four data sets. While the power-law model is disfavoured [$\chi_\nu^2 = 2.10$ for 384 degrees of freedom (d.o.f.)], the single blackbody provides an acceptable fit ($\chi_\nu^2 = 1.16$ for 384 d.o.f.); see Table 2 for the best-fitting parameters. Both double blackbody and blackbody plus power law yield similarly good fits (χ_ν^2 values of 1.10 for 376 d.o.f. and 1.12 for 376 d.o.f., respectively), but the parameters of the additional spectral components are rather unconstrained. Therefore we prefer the simplest model, a single blackbody with temperature kT changing from ∼1 to ∼0.8 keV (the derived absorbing column is $N_H \simeq 1.1 \times 10^{21}$ cm^{-2}). The corresponding observed flux decreases from ∼1.3×10^{-11} to ∼2×10^{-12} erg cm^{-2} s^{-1} (1–10 keV). These results are consistent with those reported by Cummings et al. (2009) and Göğüş, Kouveliotou & Woods (2009b), which were obtained using a smaller data set.

Although the present spectra do not allow us to discriminate among more complex (e.g. two-component or more physical) spectral models, magnetar spectra in the ∼1–10 keV range are typically described by a combination of a soft, thermal component (a blackbody) and a harder one. The latter is often represented by a nonthermal power-law tail, although in some sources a second, hotter blackbody provides an equally good (or better) interpretation (e.g. Gotthelf & Halpern 2005; Tiengo, Esposito & Mereghetti 2008). In the magnetar model, the power-law tail naturally arises from resonant cyclotron scattering (RCS) of seed thermal photons on magnetospheric currents (Thompson, Lyutikov & Kulkarni 2002). In the light of this, we attempted a simultaneous fit of all spectra with two different RCS models: the 1D model by Lyutikov & Gavriil (2006) (see also Rea et al. 2008) and the NTZ model, based on 3D Monte Carlo simulations (Nobili, Turolla & Zane 2008; Zane et al. 2009).

We tried several fits, first leaving all parameters free (except for the column density) and then assuming that either the surface temperature or some of the magnetospheric parameters is the same in all observations (the optical depth in the 1D model and the twist angle in the NTZ model). In all cases, although some fluctuations are allowed in the magnetospheric properties, we found that the best fits ($\chi_\nu^2 = 1.15$ for both models) are obtained by invoking scenarios in which the major change among the different observations is in terms of a decrease in the temperature of the thermal seed photons (from ∼0.9 to ∼0.75 keV in the 1D model and from ∼1 to ∼0.9 keV in the NTZ fits) accompanied by a decrease in the emitting surface area (of a factor of ∼4 and ∼7 in RCS and NTZ, respectively). The reprocessing of the thermal radiation by the magnetosphere is

Table 2. *Swift* spectral results for SGR 0418+5729 for the single-blackbody model. Errors are at a 1σ confidence level for a single parameter of interest. The N_H value is $1.1^{+0.1}_{-0.2} \times 10^{21}$ cm^{-2}.

Sequence	Time since t_0^a (d)	kT (keV)	Radius^b (km)	Absorbed flux^c (10^{-11} erg cm^{-2} s^{-1})
001–003	33.004–34.430	0.96 ± 0.01	0.62 ± 0.02	1.31 ± 0.03
004–007	36.156–41.121	0.94 ± 0.01	0.65 ± 0.02	1.35 ± 0.02
008–009	107.020–109.113	0.84 ± 0.02	0.43 ± 0.02	0.37 ± 0.01
010	155.164–156.098	0.83 ± 0.03	0.33 ± 0.02	0.21 ± 0.01

^{a}We assumed as t_0 MJD 54987.862, which is the time of the detection of the first burst.
^{b}The blackbody radius is calculated at infinity and for a distance of 5 kpc.
^{c}In the 1–10 keV energy range.

always quite modest, and these results are consistent with the single-blackbody fits discussed above. Overall, this favours a scenario in which heat is deposited in a spot on the neutron-star surface, following the bursting activity, that cools off and shrinks as time elapses.

3.2 *RXTE*/PCA

The analysis of the PCA spectra was mainly aimed at having flux measurements over the entire data span. We thus adopted the absorbed blackbody model and fitted it to all the PCA spectra together; the parameters were left free to vary, except for the absorption column density that was fixed at the value measured with *Swift*. Spectral channels having energies below 3 keV (standard for *RXTE* spectral analysis – see e.g. Park et al. 2004) and above 10 keV, owing to the very low signal-to-noise ratio, were ignored. This resulted in an acceptable fit ($\chi^2_\nu = 0.78$ for 644 d.o.f.) with spectral parameters similar to those reported in Table 2 (see the bottom panel of Fig. 1, but see also below for indication of a likely background contamination in these data). Again, there is a clear indication of an overall spectral softening during the decay.

We plot the resulting long-term light curve in the top panel of Fig. 1 (the last three observations provided only upper limits). The flux decays as a broken power law. Fixing $t = 0$ at the time of the detection of the first burst (2009 June 5 at 20:40:48.883 UTC; van der Horst et al. 2010), the break occurs at 17.7 ± 0.7 d, when the index changes from $\alpha_1 = -0.27 \pm 0.02$ to $\alpha_2 = -0.93 \pm 0.04$ (here and in the following, all uncertainties are at a 1σ confidence level). It is important to note that the fit parameters depend on the assumed time origin as well as on a possible steady component of the SGR flux. The uncertainties introduced by making different (reasonable) assumptions are larger than the statistical errors reported here by a factor of ∼5.

A comparison with the *Swift* flux measurements indicates a substantial discrepancy between the values derived from the XRT and the PCA instruments. This is apparent in Fig. 1 where we plotted the results from the individual *Swift*/XRT observations. While the uncertainty in the relative calibration of the two instruments (which is 10–20 per cent in the energy band considered here; Kirsch et al. 2005) cannot account for the mismatch, the fact that the difference between the *Swift*/XRT fluxes and the best-fitting curve of the *RXTE* data is consistent with being constant [$\Delta F = (1.7 \pm 0.1) \times 10^{-12}$ erg cm^{-2} s^{-1}] suggests the presence of a background contribution to the *RXTE* data. After subtracting ΔF from the *RXTE* fluxes, we fit a broken power law to the combined *RXTE* and *Swift* data, obtaining slightly different parameters for the decay: $\alpha'_1 = -0.28 \pm 0.02$, $\alpha'_2 = -1.17 \pm 0.02$ and 19.2 ± 0.4 d for the break epoch.

With respect to the flux discrepancy, we note that it is consistent with the fluctuations of the cosmic X-ray background, which in the PCA produce effects of the order of 4×10^{-12} erg cm^{-2} s^{-1} in the 2–10 keV band (Jahoda et al. 2006). We tried to better assess the situation by examining the X-ray images of the field. Apart from SGR 0418+5729, eight point sources are detected with a signal-to-noise ratio above 3 in the 2–10 keV band within the 23′-diameter FOV of the *Swift*/XRT detector. Assuming for the absorption the total Galactic value in the direction of SGR 0418+5729 ($\sim 5.6 \times 10^{21}$ cm^{-2}; see Section 8), we estimate that their total contribution to the flux observed in *RXTE* for a blackbody spectrum with $kT = 0.2$ keV is $\approx (1.5–2.5) \times 10^{-13}$ erg cm^{-2} s^{-1}, $\approx (4–6) \times 10^{-13}$ erg cm^{-2} s^{-1} for a power-law spectrum with photon index $\Gamma = 2$. Four sources outside the XRT FOV, but still in the PCA one,

are present in the Röntgen Satellite (*ROSAT*) All-Sky Survey Faint Source Catalog (Voges et al. 2000; see also Section 7); using the same assumptions as above, their 2–10 keV flux is estimated to be of $\approx (3–6) \times 10^{-14}$ erg cm^{-2} s^{-1} in the case of the blackbody spectrum and $\approx (2–5) \times 10^{-12}$ erg cm^{-2} s^{-1} for the power-law spectrum.

4 TIMING ANALYSIS

Both *RXTE*/PCA and *Swift*/XRT data were used to study the timing properties of SGR 0418+5729. We checked all observations for the presence of bursts by a careful inspection of the light curves binned with different time resolutions, but none was found. We then started the analysis of the coherent pulsations by inferring an accurate period measurement. In order to do this, we folded in the 2–10 keV band the PCA (binned at 10 d) and XRT data at the period reported by Göğüş et al. (2009a) and studied the phase evolution within the observation by means of a phase-fitting technique (details on this technique are given in Dall'Osso et al. 2003). Given the intrinsic variability of the pulse shape as a function of time, we did not make use of a pulse template to cross-correlate with. We inferred the phase of the modulation by fitting the average pulse shape of each observation with a number of sinusoids, the exact number of which is variable and determined by requesting that the addition of a further (higher) harmonic is not statistically significant (by means of an *F*-test) with respect to the null hypothesis.

The result of this analysis is reported in Fig. 2. The fit of the pulse phases with a linear component results in a reduced $\chi^2_\nu = 1.2$ for 12 d.o.f. The resulting best-fitting period is $P = 9.078\,388\,4(2)$ s (epoch 54993.0 MJD). This timing solution implies a root mean square (rms) variability of only 0.03 s. The inclusion of a quadratic term is not statistically significant, and we derive a 3σ upper limit on the first period derivative of $|\dot{P}| < 1.1 \times 10^{-13}$ s s^{-1}.

The light curve of SGR 0418+5729 in the 2–10 keV band folded at our best period is shown in Fig. 3. The pulse morphology is complex, showing two asymmetric peaks per cycle, the second of which exhibits two subpeaks. Because of the problematic background subtraction in the *RXTE*/PCA event-mode data and the possible contamination discussed in Section 3.2, here we will avoid computing pulsed fractions and hardness ratio, which are meaningful only for background-subtracted data. It is nevertheless evident that the pulse shape changes as a function of energy; one of the subpeaks is in
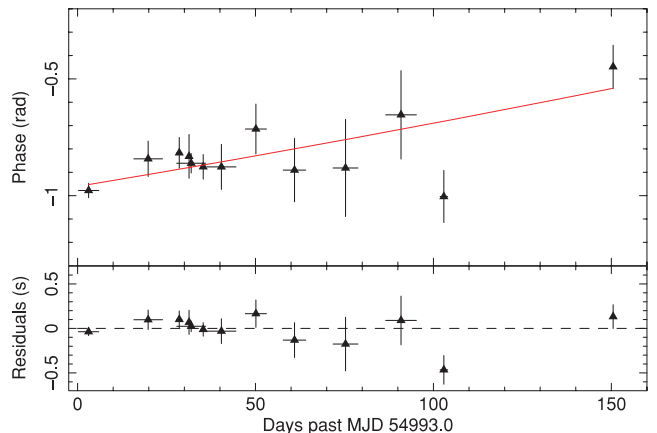

Figure 2. Top panel: 2–10 keV *RXTE*/PCA (binned at 10 d) and *Swift*/XRT pulse phase evolution with respect to the period measured by Göğüş et al. (2009a) as a function of time. The red solid line represents the phase-coherent timing solution (discussed in Section 4). Bottom panel: time residuals with respect to the timing solution.
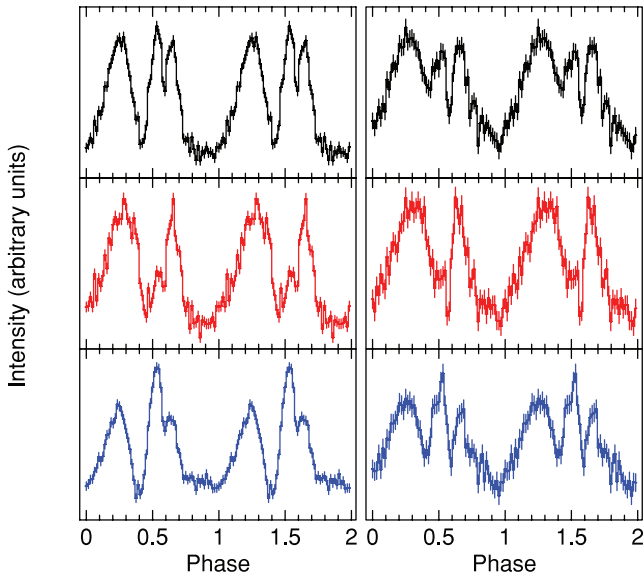
Figure 3. 64-bin *RXTE* pulse profiles before (left-hand panel) and after (right-hand panel) the break (see Fig. 1 and Section 3.2). The colours correspond to different energy bands: total (2–10 keV, top, in black), soft (2–4 keV, middle, in red) and hard (4–10 keV, bottom, in blue).

fact prominent in the hard (4–10 keV) band and nearly absent in the soft (2–4 keV) band. Furthermore, as already observed by Kuiper & Hermsen (2009), the pulse profile evolves with time. This is apparent in Fig. 3, where we show the profiles over the initial phase of the outburst and after the break at about 19 d in the decay curve (see Fig. 1 and Section 3.2).

Swift/XRT observations have lower statistics and shorter time coverage, and in the PC mode the frame time (2.5 s) does not allow us to resolve the pulse fine structures. However, the XRT data have the advantage of providing safe background subtraction and thus the measure of the pulsed fractions. To increase the statistics, we combined the observations as in Section 3. The rms pulsed fractions[3] in the 0.7–10 keV band in the four segments in chronological order are (23 ± 2), (34 ± 1), (26 ± 4) and (39 ± 6) per cent, respectively. Apart from an overall increasing trend of the pulsed fraction, which is only marginally significant (i.e. $<3\sigma$), the most substantial difference is between the values of the first two segments. We caution, however, that the poorer detailed resolution of the PC data, with respect to the WT data of the segment 004–007, can result in a smearing of the pulse profile (and hence in a reduction in the measured pulse fraction) making it difficult to compare the values.

The *Swift*-folded light curves confirm the variability of the pulse profile with energy; in particular, this is clearly visible in the high-resolution WT data shown in Fig. 4, where the pulsed fraction is (42 ± 4) per cent in the soft (1.5–2.5 keV) band and (29 ± 3) per cent in the hard (2.5–10 keV) band. To assess the statistical significance of the pulse shape variation, we compared the data using a two-sided Kolmogorov–Smirnov test (see Press et al. 1992, and references therein). The result shows that the difference between the soft and hard energy ranges is highly significant: the probability that the

---

[3] We define the pulsed fraction as $\frac{1}{\bar{y}}[\frac{1}{n}\sum_{i=1}^{n}(y_i - \bar{y})^2]^{1/2}$, where n is the number of phase bins per cycle, y_i is the number of counts in the ith phase bin and $\bar{y}$ is the mean number of counts in the cycle.
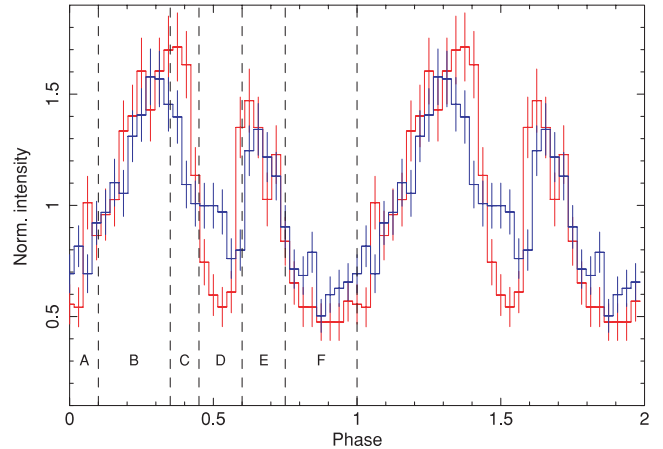

Figure 4. 32-bin *Swift*/XRT pulse profiles (background-subtracted) of SGR 0418+5729 in the 1.5–2.5 keV (red online) and 2.5–10 keV (blue online) energy ranges. The vertical dashed lines indicate the phase intervals used for the phase-resolved spectroscopy (see Section 5).

two profiles come from the same underlying distribution is in fact $\sim 1.2 \times 10^{-4}$.

5 PHASE-RESOLVED SPECTROSCOPY

To study in detail the spectral variations of SGR 0418+5729 with its pulsation phase, we extracted six spectra from the *Swift*/XRT data in the WT mode (observation 004–007) according to the phase intervals indicated in Fig. 4. We could not use the *Swift*/XRT data in the PC mode because the time resolution of this operating mode is larger than the width of the chosen phase intervals. On the other hand, the *RXTE*/PCA data are not suited either for this kind of analysis due to the large systematic uncertainties affecting the background subtraction and calibration of the PCA data with sufficient time resolution.

A simultaneous fit of these spectra with an absorbed blackbody model with only the normalization allowed to vary gives an acceptable fit ($\chi_\nu^2 = 1.15$ for 365 d.o.f.), with spectral parameters consistent with the phase-averaged spectrum. Allowing also the blackbody temperature to vary, a slightly better fit is obtained ($\chi_\nu^2 = 1.09$ for 360 d.o.f.), with the highest temperatures in phases D and F ($kT \sim 1.04$ keV) and the lowest one during phase C ($kT \sim 0.87$ keV).

We then concentrated on the two phase intervals with the largest differences, which are also apparent in the *RXTE* and *Swift* pulse profiles (Figs 3 and 4): phases C and D. A simultaneous fit of the two spectra with a single blackbody with the same temperature gives $\chi_\nu^2 = 1.26$ for 96 d.o.f., with clearly structured residuals (see Fig. 5). A slight improvement in the fit is obtained allowing for a different blackbody temperature in the two spectra ($\chi_\nu^2 = 1.12$ for 95 d.o.f.), which are $kT = 0.90^{+0.02}_{-0.03}$ keV for phase C and $kT = 1.07^{+0.02}_{-0.04}$ keV for phase D. The addition of a second blackbody gives an even better fit ($\chi_\nu^2 = 0.97$ for 91 d.o.f.), with the following best-fitting parameters [$N_H = (4 \pm 1) \times 10^{21}$ cm^{-2} for both spectra and assuming a distance of 5 kpc]: $kT_1 = 0.31^{+0.16}_{-0.06}$ keV, $R_1 = 3.4^{+1.2}_{-0.3}$ km, $kT_2 = 0.90 \pm 0.02$ keV, $R_2 = 0.79^{+0.03}_{-0.06}$ km for phase C and $kT_1 = 0.23 \pm 0.02$ keV, $R_1 = 6 \pm 2$ km, $kT_2 = 1.14^{+0.06}_{-0.04}$ keV, $R_2 = 0.43 \pm 0.04$ km for phase D. A similarly good fit ($\chi_\nu^2 = 0.99$ for 94 d.o.f.) but with a reduced number of free parameters is obtained by simultaneously fitting the two spectra with the same single absorbed blackbody model [$N_H = (7 \pm 5) \times 10^{20}$ cm^{-2}, $kT = 0.88 \pm 0.03$ keV and $R = 0.83 \pm 0.05$ km] and a
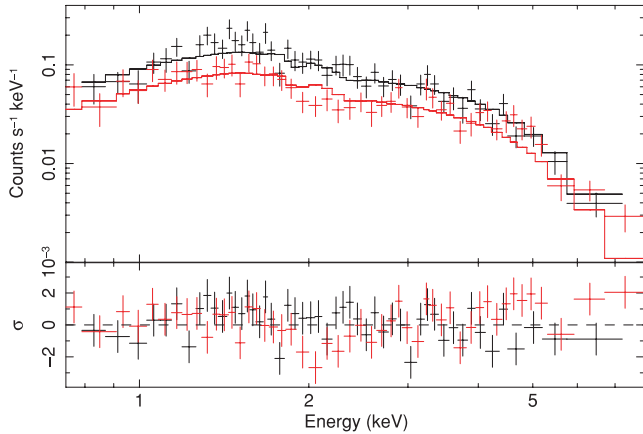
Figure 5. Phase-resolved spectroscopy of the *Swift*/XRT observations in the WT mode. Top panel: data from the phase intervals C (see Fig. 4), in black online, and D, in red online. We also plotted (solid lines) the best-fitting blackbody models (with the temperatures forced to a common value; see Section 5). Bottom panel: residuals from the models in units of standard deviations.

broad Gaussian absorption line ($E = 2.0 \pm 0.1\,\mathrm{keV}$, $\sigma_E = 1.0 \pm 0.1\,\mathrm{keV}$ and an equivalent width of 1.1 keV) only in the spectrum corresponding to phase D.

6 OPTICAL OBSERVATIONS WITH THE GRAN TELESCOPIO CANARIAS

We observed the field of SGR 0418+5729 through the Sloan i'-band filter (central wavelength $\lambda = 7800\,\text{Å}$) on 2009 September 15 (see Fig. 1) with the Optical System for Imaging and low Resolution Integrated Spectroscopy (OSIRIS; Rasilla, López López & Tejada 2008) camera mounted at the 10.4-m GTC at the Observatorio del Roque de los Muchachos in the La Palma island (Spain). OSIRIS is a two-chip CCD detector covering the wavelength range between 3650 and 10 500 Å, with a nominal FOV of $7.8 \times 8.5\,\mathrm{arcmin}^2$ which is actually decreased to $7 \times 7\,\mathrm{arcmin}^2$ due to the vignetting of chip 1. The unbinned pixel size of the CCD is 0.125 arcsec.

We took 25 dithered exposures of $\sim100\,\mathrm{s}$ each, for a total integration time of $\sim2500\,\mathrm{s}$, under dark time and with average seeing conditions of ~1.3 arcsec (airmass of 1.3–1.5). SGR 0418+5729 was positioned in chip 1, slightly offset from the CCD centre to avoid occultations from the vignetted regions during the dithered exposure sequence. To increase the signal-to-noise ratio, the exposures were taken with a 2×2 binning. Bias and dark frames were taken as daily calibrations. In particular, dark frames were taken to correct for the anomalously high dark current affecting the CCD exposures and caused by technical problems. Due to bad weather conditions, no sky flats were taken on 2009 September 15 and those taken on 2009 September 5 were used instead. Data reduction (bias and dark subtraction, flat-field correction) was performed using standard tools in the IRAF package[4] CCDRED after trimming each frame for the vignetted regions. Single dithered exposures were stacked and averaged using the task DRIZZLE which also performs the cosmic-ray filtering. Photometry calibration was performed using observations of the standard star field PG 1528+062 (Landolt 1983). The astrometry of the science frames was calibrated against the positions and coordinates of the Two-Micron All-Sky Survey
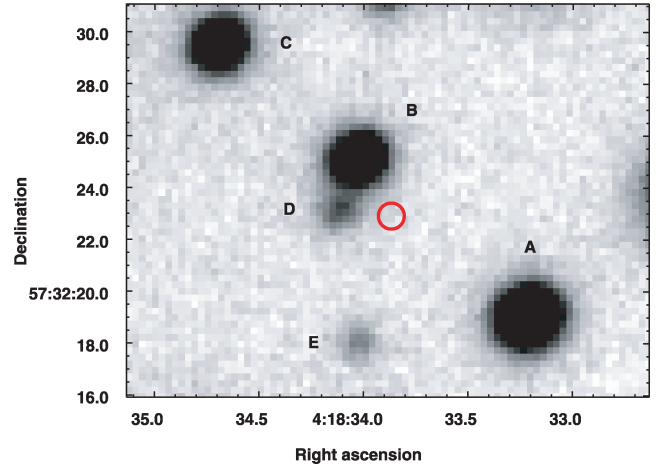

Figure 6. $20 \times 15\,\mathrm{arcsec}^2$ section of the i'-band image of the field of SGR 0418+5729 as observed by the OSIRIS camera of the GTC. North is up and east to the left. The radius (0.5 arcsec) of the error circle of SGR 0418+5729 (in red) accounts for the 0.35 arcsec uncertainty on the *Chandra* position and for the accuracy of our astrometry calibration (see Section 6). Five objects are detected in the field (labelled with capital letters); the observed apparent magnitudes of the brightest sources are: $i' = 19.536 \pm 0.004$ (A), $i' = 20.117 \pm 0.007$ (B) and $i' = 20.290 \pm 0.007$ (C). The two sources (B and D) visible north-east of the *Chandra* error circle are those detected in the K_s band by Wachter et al. (2009).

(2MASS; Skrutskie et al. 2006) stars, resulting in an overall accuracy of ~0.1 arcsec in both right ascension and declination.

The computed SGR 0418+5729 position on the OSIRIS image is shown in Fig. 6. We did not detect any source within the 95 per cent confidence *Chandra* error circle (radius of 0.35 arcsec) of SGR 0418+5729 (Woods et al. 2009b). In particular, we did not find evidence for the possible detection of the infrared source ($K_s = 21.6 \pm 1.3$ mag) tentatively seen by Wachter et al. (2009) south-west of the *Chandra* error circle on 2009 August 2, using the Wide-field InfraRed Camera (WIRC) of the Hale 5.1-m telescope at Palomar Observatory (California, USA). We set a 3σ limiting magnitude of $i' > 25.1$ on the optical brightness of SGR 0418+5729 (Mignani et al. 2009), which is the deepest obtained so far in the optical band for this source. The previous optical upper limit, obtained from observations performed with the Auxiliary-port Camera (ACAM) Imager at the 4.2-m William Herschel Telescope (WHT) on La Palma 1 month earlier, on 2009 August 16, was in fact $r > 24$ mag (Ratti, Steeghs & Jonker 2009). After de-reddening our measured upper limit using the value of the hydrogen column density derived from the X-ray spectral fits[5] (Table 2), and using the unabsorbed 1–10 keV X-ray flux measured by *Swift*/XRT (observation 008–009, which were carried out at an epoch close to the GTC observations), we infer an X-ray-to-optical flux ratio of $F_X/F_{i'} > 10\,000$ (for a bandwidth $\Delta\lambda = 1500\,\text{Å}$), in line with the ratio observed for other magnetars (e.g. Mignani 2009).

Similarly, we constrained the X-ray-to-near-infrared flux ratio using as a reference the Hale telescope observations, for which we assumed a non-detection of SGR 0418+5729 down to $K_s = 22.9$ mag. Since no *Swift*/XRT observations were obtained quasi-simultaneously to these observations, we assumed the 1–10 keV

---

[4] See http://iraf.noao.edu/.

[5] We used the relation between the N_H and the interstellar extinction A_V of Predehl & Schmitt (1995) as well as the relations between the extinctions at different wavelengths of Fitzpatrick (1999).

X-ray flux obtained from the monitoring *RXTE*/PCA observations. After de-reddening, we inferred $F_X/F_{K_s} > 50\,000$. The X-ray-to-optical flux ratio upper limit derived from WHT observations is $F_X/F_r > 3000$. The uncertainties on these ratios, mainly due to the uncertainty in the *RXTE*/PCA flux determination, are of the order of ≈ 20 per cent.

7 PRE-OUTBURST X-RAY OBSERVATIONS

There are two *ROSAT* All-Sky Survey (Voges et al. 1999) data sets containing the region of SGR 0418+5729 (sequences rs930707n00 and rs930708n00); the data were collected in the period between 1990 August 8 and 1991 February 18. The field of SGR 0418+5729 received each time roughly 530 s of exposure with the Position Sensitive Proportional Counter (PSPC; Pfeffermann et al. 1987).

SGR 0418+5729 was not detected in these data and the upper limit on the count rate, computed as the 3σ noise level due to the background at the SGR location, is about 0.05 counts s^{-1} in the 0.4–2.4 keV energy range. Using the WEBPIMMS[6] (v3.9j) tool and assuming an absorbed blackbody with $kT = 0.8$ keV and $N_H = 1.1 \times 10^{21}$ cm^{-2} (see Table 2), the limit translates into an absorbed 1–10 keV (2–10 keV) flux of $\approx 3 \times 10^{-12}$ erg cm^{-2} s^{-1} ($\approx 2 \times 10^{-12}$ erg cm^{-2} s^{-1}).

8 DISCUSSION AND CONCLUSIONS

A short period of bursting activity recently led to the discovery of the soft gamma-ray repeater SGR 0418+5729 (van der Horst et al. 2009, 2010). In the first days after the onset of the outburst, the observed flux was of a few 10^{-11} erg cm^{-2} s^{-1}, and it decreased by a factor of ~ 10 during the following 5 months. It is unknown whether the flux of SGR 0418+5729 has already decayed to (or dropped below) the pre-outburst level, since the archival (*ROSAT*) data of the field provide only an upper limit of $\approx 2 \times 10^{-12}$ erg cm^{-2} s^{-1} and magnetars often display flux variations over an order of magnitude or more (see e.g. Gotthelf & Halpern 2007; Israel et al. 2007; Esposito et al. 2008).

The X-ray data presented here allowed us to measure with accuracy the spin period of SGR 0418+5729 and to reassess the results reported in Israel et al. (2009), where a (marginally significant) period derivative of $\dot{P} = 3.0(9) \times 10^{-13}$ s s^{-1} was proposed. Now, on a longer baseline, we only infer a phase-coherent 3σ limit on the period derivative of $|\dot{P}| < 1.1 \times 10^{-13}$ s s^{-1} (valid over the range MJD 54993–55144; see Kuiper & Hermsen 2009; Woods, Göğüş & Kouveliotou 2009a for previous upper limits). The corresponding upper limits on the surface dipole magnetic field strength (inferred within the usual vacuum dipole framework; see e.g. Lorimer & Kramer 2004) and spin-down luminosity are $B \approx 3.2 \times 10^{19}(P\dot{P})^{1/2} < 3 \times 10^{13}$ G and $\dot{E} = 4\pi^2 I\dot{P}P^{-3} < 6 \times 10^{30}$ erg s^{-1}, respectively, where $I \simeq 10^{45}$ g cm^2 is the moment of inertia of a neutron star. The properties inferred from the period derivative should be taken with additional caution for magnetars, since their spin-down rates can be highly variable. Nevertheless, the present limits on B and $\dot{E}$ for SGR 0418+5729 are the lowest values among magnetars (see e.g. fig. 2 of Esposito et al. 2009), 1E 2259+586 being the closest, with $B \simeq 6 \times 10^{13}$ G and $\dot{E} \simeq 5.6 \times 10^{31}$ erg s^{-1} (Gavriil & Kaspi 2002).

The distance of SGR 0418+5729 is not known yet; however, considering the structure of the Galaxy proposed by Hou, Han &

Shi (2009), the Galactic coordinates of the SGR ($l = 147°.98$ and $b = 5°.12$) suggest that it is located within a distance smaller than ≈ 5 kpc. van der Horst et al. (2010) assume a distance of ~ 2 kpc in the hypothesis that SGR 0418+5729 is situated in the Perseus arm of the Galaxy. Such a relatively small distance is consistent with the measure of the photoabsorption derived from the X-ray spectral analysis ($N_H \simeq 1.1 \times 10^{21}$ cm^{-2}; see Table 2). This value is in fact significantly smaller than the total Galactic interstellar hydrogen along the line of sight which can be estimated from the Leiden/Argentine/Bonn (LAB) survey of H I (Kalberla et al. 2005) and the CO survey of Dame, Hartmann & Thaddeus (2001) for the value of molecular H_2 as $N_H = N_{HI} + 2N_{H_2} = (4.30 + 2 \times 0.67) \times 10^{21}$ cm$^{-2} \simeq 5.6 \times 10^{21}$ cm^{-2}.

Conservatively assuming a distance of 5 kpc, the 1–10 keV X-ray luminosity measured with *Swift* varied during the outburst from $L_X \simeq 4 \times 10^{34}$ to 6×10^{33} erg s^{-1}. The minimum observed ratio between the luminosity and the spin-down energy loss is $L_X/\dot{E} > 10^3 d_5^2$, where d_N indicates the distance in units of N kpc, a value which, when compared to those of other magnetar sources, fully qualifies SGR 0418+5729 as a member of the magnetar class.

The upper limit on the period derivative corresponds, in the standard magneto-dipole braking model, to a characteristic age $\tau_c = P/(2\dot{P}) > 1.1$ Myr, the highest (so far) among magnetars. The location of SGR 0418+5729 on the P–$\dot{P}$ diagram (see e.g. fig. 4 of McLaughlin et al. 2009 for an updated diagram) falls quite close to the region of the X-ray dim isolated neutron stars (XDINSs; see Turolla 2009 for a review), often proposed to be evolved magnetars on the basis of their comparable spin periods and relatively large dipole magnetic fields. Although age estimates based on the magneto-dipole model are highly uncertain[7] it is intriguing to think SGR 0418+5729 as an 'old magnetar' (or a young XDINS), ideally linking the two classes of isolated neutron stars.

We performed the spectral analysis of the *Swift* observations of SGR 0418+5729 by assuming different phenomenological models (combinations of blackbodies and power laws) or more complex ones, based on the RCS of seed surface photons by magnetospheric currents (1D and NTZ models). In all cases, we found that *Swift* data are compatible with a scenario in which the flux decrease is mainly due to the cooling and shrinking of a hot emitting region on the neutron-star surface, which may have been suddenly heated following the bursting activity. This is in agreement with what is observed in the post-outburst evolution of other transient magnetars (e.g. Gotthelf & Halpern 2005). SGR 0501+4516 is the only other repeater for which the outburst decay has been monitored with detailed, quasi-continuous observations (*XMM–Newton* and *Swift*) over a time-span (~ 160 d) comparable to the present one (Rea et al. 2009). In that case, however, the flux decline was exponential with a time-scale of ~ 24 d and there was no evidence for a power-law decay. The first *Swift* observation was performed only 33 d after the onset of the bursting phase and by that time one may expect that major deviations from a dipolar magnetosphere have died away (see e.g. Esposito et al. 2008), leaving only a cooling hotspot at the neutron-star surface as the relic of the outburst. Alternatively, the twisted portion of the magnetosphere could have been quite small, as suggested by Beloborodov (2009) in the case of the AXP XTE J1810−197, making it difficult for thermal photons to resonantly scatter on to magnetospheric currents.

---

[6] See http://heasarc.gsfc.nasa.gov/Tools/w3pimms.html.

[7] An independent age estimate could come from the association with a supernova remnant. However, there are no known remnants within $2°$ from SGR 0418+5729.

RXTE pulse profiles (and, to a lesser extent because of the lower count statistics, also *Swift* ones) exhibit a complex pattern, with an overall double-peaked shape. If we assume that emission mainly comes from the star surface with little contribution from the magnetosphere (see the above discussion) and it is essentially isotropic,[8] double-peaked light curves arise when the angles ξ, between the line connecting the two (antipodal) emitting spots and the rotation axis, and χ, between the line of sight and the rotation axis, are such that $\xi + \chi \gtrsim 120°$ for a radius $R_{NS} \sim 3R_S$ (here, R_S is the Schwarzschild radius; e.g. Beloborodov 2002; Poutanen & Beloborodov 2006). This suggests that SGR 0418+5729 is a nearly orthogonal rotator seen at a large inclination angle. Pulse profiles are both energy- and time-dependent, with evidence for a hard (>4 keV) component concentrated near the second light maximum (phase of $\sim$0.6), which becomes less prominent as the flux declines (see Fig. 3). This, again, points to a picture in which only a limited portion of the star surface has been heated as a consequence of the event which produced the outburst. The near-coincidence in phase of the (second) soft and hard peaks, together with the decrease of the latter at later times, may indicate that heating involved only one of the two spots, e.g. producing a hotter region inside (or close to) one of the warm polar caps.

Phase-resolved spectroscopy of the (combined) *Swift* WT data shows that emission near the phase intervals of maximum softness/hardness is described well by the superposition of two blackbodies with different radii and temperatures in each interval. The radii of the two cooler blackbodies are not much different and, although somewhat too small ($\approx$4–6 km), might be associated with the neutron-star radius, while their temperatures are quite close and consistent with being the same within the errors. A possibility, then, is that emission comes from two spots at different temperatures, while the rest of the surface is at a lower temperature. Phase-resolved spectral fits suggest two other options: two emitting regions, each comprising a hotter inner cap and a surrounding warmer corona, and two equal spots, one of which emits a blackbody plus a Gaussian absorption feature. In both these scenarios, the rest of the surface is likely to be rather colder than the lower temperature obtained from the blackbody fit. A preliminary calculation indicates that all these configurations can produce pulse profiles which are in general agreement with the observed ones.

After the outburst, the flux of SGR 0418+5729 follows a broken power-law decay, $F \propto t^\alpha$, with a break at $\sim$19 d and $\alpha_1 \sim -0.3$, $\alpha_2 \sim -1.2$ (for the fit to the combined *RXTE* and *Swift* data; see Section 3.2). The post-outburst cooling of magnetars has been modelled in terms of a sudden heat deposition in the neutron-star crustal layers, due to the release of energy stored in the toroidal component of the internal magnetic field (Lyubarsky, Eichler & Thompson 2002; see also Kouveliotou et al. 2003). In this picture the flux decays as $F \propto t^{-n/3}$, with $n \sim 2$–3. While the predicted index might account for the flux evolution in SGR 0418+5729 after the break, it is inconsistent with what is observed before the break, and, even more important, the model does not predict any change of slope during the decay. On the other hand, it should be stressed that the calculation of Lyubarsky et al. (2002) was mainly aimed at explaining the flux decay in SGR 1900+14 after its giant flare and consequently assumes a magnetic field $B \sim 10^{15}$ G. According-

ing to the limit on $\dot{P}$ presented in Section 4, the magnetic field of SGR 0418+5729 is likely to be two orders of magnitude lower, so the model may not be directly applicable in this case.

A different possibility is that the surface layers of the star are heated by returning currents that flow along the closed field lines of a twisted magnetosphere (Thompson et al. 2002; Beloborodov & Thompson 2007; Beloborodov 2009). The twist is likely to be localized into a small bundle of current-carrying field lines (the *j*-bundle) close to the magnetic pole and must decay in order to supply its own supporting currents. As the magnetosphere untwists, the angular extent of the *j*-bundle decreases, the luminosity decays and the area hit by the currents shrinks (Beloborodov 2009). The details of the evolution depend on the initial distribution of the twist inside the *j*-bundle, and no general law for the luminosity decay exists. If the twisted region is small, the emergent spectrum is dominated by emission from the heated cap and it is thermal because photons do not have many chances to scatter. The flux is then $F \propto R^2 T^4$, where R and T are the radius and temperature of the cap, respectively. The decay of the temperature (as derived from the single-blackbody fits to *RXTE* and *Swift* data) is reasonably well described by a single power law, $T \propto t^{-0.05}$ (see Fig. 1), over the entire time-span, without the need to introduce a break. If the temperature variation is entirely due to the cooling of a cap, the emitting area decreases as $R^2 \propto t^{-0.08}$ and $R^2 \propto t^{-0.97}$ before and after the break, respectively. If the single-blackbody model mostly traces the emission from the hot region, as it seems reasonable also from the comparison of the fit parameters with those of the hotter component in the two-blackbody model (see Table 2 and Section 5), it follows that, after the break, the radius of the cap scales as $t^{-0.41}$, close enough to the dependence derived above ($R \propto t^{-0.48}$). A better estimate of the cap radius could come from the two-blackbody model, but the limited statistics allows its application only to the combined *Swift* observations, taken at different epochs after the break. Assuming as a rough estimate that the hottest blackbody radius $R_2 \sim 0.43$ km can be associated with $t \sim 35$ d, around which five observations cluster, the source luminosity is $L \sim 4 \times 10^{34} d_5^2$ erg s^{-1}. This value is too high to be explained by the rate of Ohmic dissipation, $L \approx 10^{36}(B/10^{14}$ G$)(R_{NS}/10^6$ cm$)\psi$ $(V/10^9$ V$)\sin^4\theta_*$ erg s^{-1} (here, $\psi \lesssim 1$ rad is the twist angle and V is the discharge voltage; Beloborodov 2009), if the magnetic field is $\sim 10^{13}$ G and the angular size of the twist is $\sin \theta_* \sim R_2/R_{NS} \sim 0.03$. The problem is however eased for a larger cap area, as in the case in which the cap contains a small hot region surrounded by a warm corona.

Currently, several AXPs and SGRs have been firmly identified also at optical and/or infrared wavelengths (see Mignani 2009, and references therein). However, there are no detailed predictions yet about the X-ray-to-optical (or infrared) flux ratio that a magnetar is expected to have. Our deep GTC *i'* observation of SGR 0418+5729 points to an X-ray-to-optical flux ratio exceeding 10^4, a value not unheard of among magnetars (e.g. Mignani 2009). The GTC image adds a new piece to the still sparse – but growing – data base of optical/infrared observations of magnetars exploring a range of different states of high energy activity. Enlarging such a data base is indeed a farsighted effort since it will be the only way to decipher the nature of magnetar optical/infrared emission and of its correlation with the high energy emission.

---

[8] We warn that this is an oversimplification since thermal emission from a magnetized neutron star, from either an atmosphere or a condensed surface, is not isotropic (e.g. Zavlin et al. 1995; Turolla, Zane & Drake 2004).

REFERENCES

Anders E., Grevesse N., 1989, Geochim. Cosmochim. Acta, 53, 197

Arnaud K. A., 1996, in Jacoby G. H., Barnes J., eds, ASP Conf. Ser. Vol. 101, Astronomical Data Analysis Software and Systems V. Astron. Soc. Pac., San Francisco, p. 17

Balucinska-Church M., McCammon D., 1992, ApJ, 400, 699

Beloborodov A. M., 2002, ApJ, 566, L85

Beloborodov A. M., 2009, ApJ, 703, 1044

Beloborodov A. M., Thompson C., 2007, ApJ, 657, 967

Burrows D. N. et al., 2005, Space Sci. Rev., 120, 165

Cummings J. R., Page K. L., Beardmore A. P., Gehrels N., 2009, Astron. Telegram, 2127

Dall'Osso S., Israel G. L., Stella L., Possenti A., Perozzi E., 2003, ApJ, 599, 485

Dame T. M., Hartmann D., Thaddeus P., 2001, ApJ, 547, 792

Duncan R. C., Thompson C., 1992, ApJ, 392, L9

Esposito P. et al., 2008, MNRAS, 390, L34

Esposito P. et al., 2009, MNRAS, 399, L44

Fitzpatrick E. L., 1999, PASP, 111, 63

Gavriil F. P., Kaspi V. M., 2002, ApJ, 567, 1067

Göğüş E., Woods P., Kouveliotou C., 2009a, Astron. Telegram, 2076

Göğüş E., Kouveliotou C., Woods P. M., 2009b, Astron. Telegram, 2121

Gotthelf E. V., Halpern J. P., 2005, ApJ, 632, 1075

Gotthelf E. V., Halpern J. P., 2007, Ap&SS, 308, 79

Hill J. E. et al., 2004, in Flanagan K. A., Siegmund O. H. W., eds, Proc. SPIE Conf. Ser. Vol. 5165, X-ray and Gamma-ray Instrumentation for Astronomy XIII. SPIE, Bellingham, p. 217

Hou L. G., Han J. L., Shi W. B., 2009, A&A, 499, 473

Hurley K. et al., 2005, Nat, 434, 1098

Israel G. L., Campana S., Dall'Osso S., Muno M. P., Cummings J., Perna R., Stella L., 2007, ApJ, 664, 448

Israel G. L., Esposito P., Götz D., Rea N., 2009, Astron. Telegram, 2209

Jahoda K., Swank J. H., Giles A. B., Stark M. J., Strohmayer T., Zhang W., Morgan E. H., 1996, in Siegmund O. H. W., Gummin M. A., eds, Proc. SPIE Conf. Ser. Vol. 2808, EUV, X-Ray, and Gamma-Ray Instrumentation for Astronomy VII. SPIE, Bellingham, p. 59

Jahoda K., Markwardt C. B., Radeva Y., Rots A. H., Stark M. J., Swank J. H., Strohmayer T. E., Zhang W., 2006, ApJS, 163, 401

Kalberla P. M. W., Burton W. B., Hartmann D., Arnal E. M., Bajaja E., Morras R., Pöppel W. G. L., 2005, A&A, 440, 775

Kirsch M. G. et al., 2005, in Siegmund O. H. W., ed., Proc. SPIE Conf. Ser. Vol. 5898, UV, X-Ray, and Gamma-Ray Space Instrumentation for Astronomy XIV. SPIE, Bellingham, p. 22

Kouveliotou C. et al., 2003, ApJ, 596, L79

Kuiper L., Hermsen W., 2009, Astron. Telegram, 2151

Landolt A. U., 1983, AJ, 88, 439

Lorimer D. R., Kramer M., 2004, Handbook of Pulsar Astronomy. Cambridge Univ. Press, Cambridge

Lorimer D. R., Edel S., Kondratiev V. I., McLaughlin M. A., Boyles J. R., Ludovici D. A., Ridley J. P., 2009, Astron. Telegram, 2096

Lyubarsky Y., Eichler D., Thompson C., 2002, ApJ, 580, L69

Lyutikov M., Gavriil F. P., 2006, MNRAS, 368, 690

McLaughlin M. A. et al., 2009, MNRAS, 400, 1431

Mereghetti S., 2008, A&AR, 15, 225

Mignani R. P., 2009, Advances Space Res., in press, preprint (astro-ph/0912.2931)

Mignani R. P. et al., 2009, Astron. Telegram, 2244

Nobili L., Turolla R., Zane S., 2008, MNRAS, 386, 1527

Paczynski B., 1992, Acta Astron., 42, 145

Park S. Q. et al., 2004, ApJ, 610, 378

Pfeffermann E. et al., 1987, in Koch E.-E., Schmahl G., eds, Proc. SPIE Conf. Ser. Vol. 733, Soft X-ray Optics and Technology. SPIE, Bellingham, p. 519

Poutanen J., Beloborodov A. M., 2006, MNRAS, 373, 836

Predehl P., Schmitt J. H. M. M., 1995, A&A, 293, 889

Press W. H., Teukolsky S. A., Vetterling W. T., Flannery B. P., 1992, Numerical Recipes in C. The Art of Scientific Computing, 2nd edn. Cambridge Univ. Press, Cambridge

Rasilla J. L., López López R., Tejada C., 2008, in McLean, Ian S., Casali, Mark M., eds, Proc. SPIE Conf. Ser. Vol. 7014, Ground-Based and Airborne Instrumentation for Astronomy II. SPIE, Bellingham, p. 701438

Ratti E., Steeghs D., Jonker P. G., 2009, Astron. Telegram, 2169

Rea N., Zane S., Turolla R., Lyutikov M., Götz D., 2008, ApJ, 686, 1245

Rea N. et al., 2009, MNRAS, 396, 2419

Skrutskie M. F. et al., 2006, AJ, 131, 1163

Thompson C., Duncan R. C., 1995, MNRAS, 275, 255

Thompson C., Duncan R. C., 1996, ApJ, 473, 322

Thompson C., Lyutikov M., Kulkarni S. R., 2002, ApJ, 574, 332

Tiengo A., Esposito P., Mereghetti S., 2008, ApJ, 680, L133

Turolla R., 2009, in Becker W., ed., Astrophysics and Space Science Library Vol. 357, Neutron Stars and Pulsars. Springer, Berlin, p. 141

Turolla R., Zane S., Drake J. J., 2004, ApJ, 603, 265

van der Horst A. J. et al., 2010, ApJ, 711, L1

van der Horst A. J. et al., 2009, Astron. Telegram, 2077

Voges W. et al., 1999, A&A, 349, 389

Voges W. et al., 2000, IAU Circular, 7432, 3

Wachter S., Gelino C. R., Gelino D. M., Woods P., Kouveliotou C., Göğüş E., 2009, Astron. Telegram, 2164

Woods P. M., Thompson C., 2006, in Levin W. H. G., van der Klis M., eds, Compact Stellar X-Ray Sources. Cambridge Univ. Press, Cambridge, p. 547

Woods P. M., Göğüş E., Kouveliotou C., 2009a, Astron. Telegram, 2152

Woods P. M., Wachter S., Göğüş E., Kouveliotou C., 2009b, Astron. Telegram, 2159

Zane S., Rea N., Turolla R., Nobili L., 2009, MNRAS, 398, 1403

Zavlin V. E., Pavlov G. G., Shibanov Y. A., Ventura J., 1995, A&A, 297, 441

This paper has been typeset from a TEX/LATEX file prepared by the author.